A Contact Binary Misclassified as an Ellipsoidal Variable: Complications for Detached Black Hole Searches

Tyrone N. O'Doherty[1] , Arash Bahramian[1] , Adelle J. Goodwin[1] , James C. A. Miller-Jones[1] , Jerome A. Orosz[2] , and Jay Strader[3]

[1] International Centre for Radio Astronomy Research—Curtin University, GPO Box U1987, Perth, WA 6845, Australia; tyrone.odoherty@postgrad.curtin.edu.au
[2] Department of Astronomy, San Diego State University, 5500 Campanile Drive, San Diego, CA 92182, USA
[3] Center for Data Intensive and Time Domain Astronomy, Department of Physics and Astronomy, Michigan State University, East Lansing, MI 48824, USA

Abstract

Identifying sources exhibiting ellipsoidal variability in large photometric surveys is becoming a promising method to search for candidate detached black holes (BHs) in binaries. This technique aims to exploit the orbital-phase-dependent modulation in optical photometry caused by the BH distorting the shape of the luminous star to constrain the mass ratio of the binary. Without understanding if, or how much, contamination is present in the candidate BH samples produced by this new technique it is hard to leverage them for BH discovery. Here, we follow up one of the best candidates identified from Gaia Data Release 3, Gaia DR3 4042390512917208960, with a radial velocity (RV) campaign. Combined photometric and RV modeling, along with spectral disentangling, suggests that the true mass ratio (the mass of the unseen object divided by the mass of the luminous star) is an order of magnitude smaller than that inferred assuming the modulations arise from ellipsoidal variability. We therefore infer that this system is likely a contact binary, or on the boundary of both stars nearly filling their Roche lobes; however, further observations are required to confidently detect the secondary. We find that the well-known problem of discriminating between ellipsoidal and contact binary light curves results in a larger contamination from contact binaries than previously suggested. Until ellipsoidal variables can be reliably distinguished from contact binaries, samples of BH candidates selected based on ellipsoidal variability are likely to be highly contaminated by contact binaries or similar systems.

Unified Astronomy Thesaurus concepts: Stellar mass black holes (1611); Ellipsoidal variable stars (455); Close binary stars (254); Contact binary stars (297); Spectroscopy (1558)

1. Introduction

The Milky Way is expected to contain 10^8–10^9 stellar-mass black holes (BHs) based on current stellar evolution theories (e.g., van den Heuvel 1992; Brown & Bethe 1994; Timmes et al. 1996; Samland 1998; Wiktorowicz et al. 2019; Olejak et al. 2020). However, it is challenging to constrain this population observationally. So far, the only method that has proven successful in identifying isolated BHs is through gravitational microlensing, the first of which was confirmed only recently (Lam et al. 2022a, 2022b; Sahu et al. 2022). The occurrence of microlensing by isolated BHs is unpredictable, and these events cannot be followed up once the event is over. As a result, studies often focus on looking for BHs in binary systems. Until very recently, the vast majority of confirmed and candidate Galactic BHs came from X-ray binaries (XRBs; e.g., Corral-Santana et al. 2016; Tetarenko et al. 2016). XRBs are binary systems in which a BH accretes from a stellar companion, and in the process radiates liberated gravitational potential energy. These XRBs are primarily identified through X-ray emission arising from accretion. However, broadly, this means the discovery of BHs has been limited to systems in a configuration favorable to accretion. Furthermore, the discovery of transient accreting BHs, which make up the majority, is limited to systems with short recurrence timescales (X-ray all-sky surveys have only been running for several decades). While accreting BHs make up the majority of the known population of Galactic BHs, it is believed that they are only a small component of the total Galactic BH population (e.g., van den Heuvel 1992; Corral-Santana et al. 2016).

Identifying detached BHs in binary systems in the Galaxy has been the focus of numerous studies over the last decade. Of the many initially promising candidates, very few have been found to actually host a BH. While there are ∼20 accreting Galactic BHs with dynamical mass estimates (Corral-Santana et al. 2016; Tetarenko et al. 2016), there are only five confirmed Galactic detached systems with dynamical mass estimates that cannot accommodate a neutron star (NS) in configurations where a nondegenerate companion is infeasible. These are the two BHs discovered in the globular cluster NGC 3201 by a spectral survey (Giesers et al. 2018, 2019), two BHs in the Galactic field (Tanikawa et al. 2023; El-Badry et al. 2023a, 2023b; Shahaf et al. 2023) initially identified using binary astrometric solutions from Gaia Data Release 3 (DR3; Gaia Collaboration et al. 2016, 2023), and one system discovered through a spectroscopic survey of Galactic O-type stars (Mahy et al. 2022). A sixth possible detached BH is 2MASS J05215658+4359220 (Thompson et al. 2019, 2020), although while a BH seems likely, the lower limit of the mass estimate ($M = 3.3^{+2.8}_{-0.7}$ $M_\odot$; Thompson et al. 2020) does not conclusively rule out a NS due to uncertainties in the NS equation of state. A possible seventh detached BH is NGC 1850 BH1 (El-Badry & Burdge 2022; Saracino et al. 2022, 2023; Stevance et al. 2022), however work is still ongoing. This means that in the Galactic field there are only

three, possibly four, known detached BHs thus far. Developing methods of reliably identifying new BH candidates is critical for discovering more of this elusive population.

The all-sky astrometric, photometric, and spectroscopic Gaia mission is providing a wealth of data in which to search for detached BHs. Indeed, two of the confirmed detached BHs in the Galactic field come from an analysis of the astrometric orbits provided with DR3. However, while there are ∼2 billion sources in DR3, there are only ∼1 million binary orbital solutions. There are likely many more sources with detached BH companions that have been observed by Gaia that are yet to be identified. While novel techniques have been used to identify promising candidates from Gaia (e.g., Andrew et al. 2022; Gomel et al. 2023), it is not understood if, or how much, contamination from non-BH systems is present in these samples. Without understanding this possible contamination, it is hard to exploit these new techniques to their full potential. Following up candidates identified using Gaia with spectroscopic radial velocity (RV) studies has the potential to substantially increase the known sample of detached BH systems, as well as helping to understand the contamination present in these samples and thereby refine the selection techniques.

Accompanying the release of DR3 were papers detailing the analysis of numerous kinds of variable sources and their classification (see, e.g., Eyer et al. 2023; Gavras et al. 2023; Rimoldini et al. 2023, and references therein). This includes ellipsoidal variables, which were used to identify candidate binaries with compact companions (Gomel et al. 2023). In binary systems, the gravity of each component acts on the other, distorting their shape. In BH–star binaries the BH can significantly distort the star into a teardrop shape, resulting in sinusoidal modulations of the observed luminosity of the star on the orbital period. Gomel et al. (2021a) determined a relationship for a "modified minimum mass ratio" (mMMR) that can be computed from the light-curve modulation, and does not depend on the mass and radius of the visible star. This mMMR was found to always be less than the minimum mass ratio, which is in turn less than the true mass ratio ($q = M_{BH}/M_{star}$). The main physical assumptions underlying the derived relationship are that the primary star fills its Roche lobe and that the binary has an inclination of 90° (deviations from these assumptions imply the true mass ratio is larger than the mMMR). The other main assumption is that the light is coming from the primary star only. This method was applied to the variable sources identified as ellipsoidal variables by the Gaia Variability Pipeline (Eyer et al. 2023) classifier (Rimoldini et al. 2023), producing 6306 detached or weakly accreting BH and NS candidates.

The 6306 candidates identified by Gomel et al. (2023) are a large sample, and if all are real would represent a substantial increase to the known populations of BHs and NSs. However, as there is likely some level of contamination from systems like contact binaries (Gomel et al. 2023), follow-up is required. This work builds on that carried out by Nagarajan et al. (2023), who followed up 14 systems from Gomel et al. (2023) and found they were unlikely to contain BHs, but did not conclusively characterize the systems. In this paper, we investigate one of the most promising BH candidates from the Gomel et al. (2023) sample and discuss the results of our spectroscopic and photometric modeling that reveal it is likely a contact binary. In Section 2.1, we discuss the selection of this

source for targeted follow-up and the details of the spectroscopic campaign. Details of the RV extraction and modeling, joint photometric and RV modeling, spectral disentangling, and the associated results of the analysis are presented in Section 3. The results are discussed in Section 4.

2. Observations

2.1. Source Selection

We began by filtering the 6306 candidates from Gomel et al. (2023), retaining sources for which we could estimate a reliable distance and with no evidence of a luminous companion in Gaia. These restrictions manifested as a cut on parallax significance greater than 3 and requiring the Gaia parameter IPD_MULTI_FRAC = 0 (the fraction of successful windows in which their fitting algorithm identified a double peak, and thus potentially a resolved double star, be it a true binary or a visual double). From here, we began exploration by restricting mMMR to be at least 2, leaving a sample of 13 sources. From this sample of 13, there is one particularly interesting source: Gaia DR3 4042390512917208960.

Gaia DR3 4042390512917208960 has a mMMR of 2.54 (1.78 at 1σ). The mass estimated by the Gaia team for the luminous star by leveraging astrometry, photometry, and spectroscopy is $1.809^{+0.058}_{-0.054} M_\odot$ (Creevey et al. 2023; Fouesneau et al. 2023). Assuming this mass is correct, the inferred mass of the unseen object is $>4.6 M_\odot$ ($>3 M_\odot$ at 1σ), making it an excellent BH candidate. This source is one of 262 sources with mMMR significantly higher than 1, which were identified by Gomel et al. (2023) as being the most promising BH candidates. Furthermore, it is bright ($G = 13.8$), making spectroscopic follow-up feasible with a wide range of instruments.

Gaia DR3 4042390512917208960 has excellent astrometry (Lindegren et al. 2021), with a parallax significance greater than 20. The renormalized unit weight error (RUWE) for this source is 0.707, suggestive of overfitting. Other astrometric goodness-of-fit statistics (e.g., astrometic excess noise, and all image parameter determination statistics) are as expected for a well-behaved system. A RUWE of 0.707 is therefore likely not a cause for concern. The blue and red photometric excess factor is 1.235, however this excess is fully consistent with the excess seen in standard sources (see Figure 18 in Riello et al. 2021). The *Gaia* G, G_{RP}, and G_{BP} phase-folded photometry can be found in Figure 1. The photometry was extracted from the Gaia archive.[4] Sinusoidal modulation can clearly be seen in all colors. However, the modulation is not completely smooth, showing some scatter. We think this is likely a result of contamination, which is not unexpected given the source's location in the bulge. Approximately 20% of the source's transits of the Gaia field of view were marked as blended, ((PHOT_BP_N_BLENDED_TRANSITS+PHOT_RP_N_BLEN-DED_TRANSITS)/(PHOT_RP_N_OBS+PHOT_BP_N_OBS)), where a blended transit means that there was at least one more source in the observing window (Riello et al. 2021). It is important to note that a blended transit occurring is dependent on the scan direction, and thus different transits of the same source can be blended in different ways or not at all (Riello et al. 2021). However, the scatter does not significantly alter the general shape of the sinusoidal modulation. In summary, the
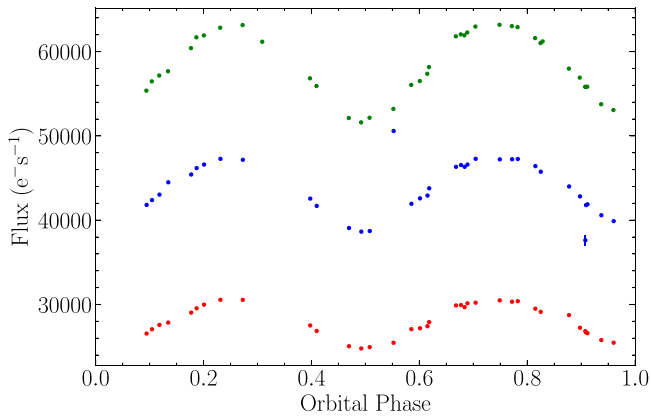
---

4   https://gea.esac.esa.int/archive/

Figure 1. Phase-folded Gaia G, G_{RP}, and G_{BP} photometry of Gaia DR3 4042390512917208960. The smooth sinusoidal modulation is evident in all colors.

Figure 2. Phase-folded OGLE I-band photometry. The same shape can be seen as in Figure 1.

Gaia astrometric and photometric solution is believable and raises no major concerns.

It is worth noting that this source lies slightly above the main sequence (see Figure 6 in Gomel et al. 2023), which could arise from the unseen companion being a luminous object. It is possible to hide a more massive stellar secondary in systems with evolved stars (e.g., El-Badry et al. 2022). However, the luminous star in Gaia DR3 4042390512917208960 shows no evidence of being significantly evolved off the main sequence (Fouesneau et al. 2023). Furthermore, the estimated mass of the unseen object is large enough such that its luminosity contribution (if it is a main-sequence star) would be significant. Cumulatively, as also identified by Gomel et al. (2023), we identified this source as an interesting candidate and worthy of further study.

2.2. Archival Observations of Gaia DR3 4042390512917208960

The location and brightness of Gaia DR3 4042390512917208960 means it has been observed by both the Optical Gravitational Lensing Experiment (OGLE; Udalski et al. 2015) and the All-Sky Automated Survey for Supernovae (ASAS-SN; Shappee et al. 2014; Kochanek et al. 2017). The OGLE I-band photometry was extracted from the OGLE Collection of Variable Stars online database, and is presented in Figure 2.[5] It was classified as an ellipsoidal variable by OGLE (OGLE BLG-ELL-012306; Soszyński et al. 2016). In their study of OGLE ellipsoidal variables in the Galactic bulge, Gomel et al. (2021b) derived a similar mMMR, also noting it as an interesting candidate. However, the ASAS-SN V team's machine-learning classifier classed it as an eclipsing contact binary (ASASSN-V J175613.02-335233.3; Jayasinghe et al. 2020). Note that ellipsoidal variable was not a classification category in Jayasinghe et al. (2020). Later, Rowan et al. (2021) searched for ellipsoidal variables within ASAS-SN data using a combined χ^2 ratio test followed by visual inspection, identifying 369 candidates. However, ASASSN-V J175613.02-335233.3 was not identified as an ellipsoidal candidate in this study. Gomel et al. (2023) suggested that it is an ellipsoidal variable based on the Gaia and OGLE classification. They also suggested that the comparatively low
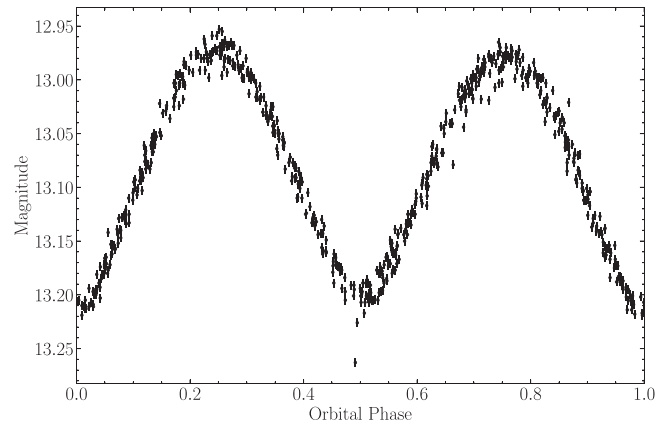
amplitude of the modulation observed by ASAS-SN arises from contamination as the source is in the Galactic bulge.

2.3. Dedicated Spectroscopic Follow-up

We obtained spectroscopic observations of Gaia DR3 4042390512917208960 using the Wide Field Spectrograph (WiFeS; Dopita et al. 2007, 2010), an integral field unit (IFU) spectrograph on the Australian National University 2.3 m optical telescope. The spectrograph has both a "blue" and a "red" camera, with which we used the "B7000" and "R7000" gratings ($R \sim 7000$) offering simultaneous wavelength coverage of 4184–5580 Å and 5294–7060 Å, respectively. Ne–Ar arc-lamp exposures were taken immediately following each science observation for wavelength calibration. Data were reduced using the PyWiFeS pipeline (Childress et al. 2014).[6] Data were taken between 2022 June 23 and 2023 April 19 for a total of 24 observations. Individual observations were taken with two 700 s exposures (separated temporally only by readout time) so that the duration of each exposure was less than 1% of the orbit of the binary ($P_{orb} = 0.8952134$ day; Soszyński et al. 2016). Resultant spectra typically have a signal-to-noise ratio of >250 per resolution element in the continuum.

We obtained a single 300 s spectrum of the source with the Goodman Spectrograph (Clemens et al. 2004) on the SOAR telescope on 2022 October 30. This spectrum used the $2100 \, 1 \, mm^{-1}$ grating and a $1.''2$ longslit, giving a FWHM resolution of about 0.9 Å over the wavelength range 6090–6660 Å. The spectrum was optimally extracted and wavelength calibrated with a time-adjacent arc-lamp exposure using standard tools in IRAF (Tody 1986), with a signal-to-noise of ~ 85 per resolution element in the continuum.

3. Analysis and Results

3.1. Radial Velocity Estimation

The output of the PyWiFeS pipeline is a calibrated data cube with a spectrum (frequency and brightness) for each pixel in the IFU. We extracted spectra of Gaia DR3 4042390512917208960 from pixels of the WiFeS IFU centered on the source whose total flux was greater than 5 times the rms flux of background pixels, followed by a subtraction of an

---

[5] https://ogledb.astrouw.edu.pl/~ogle/OCVS/ecl_query.php
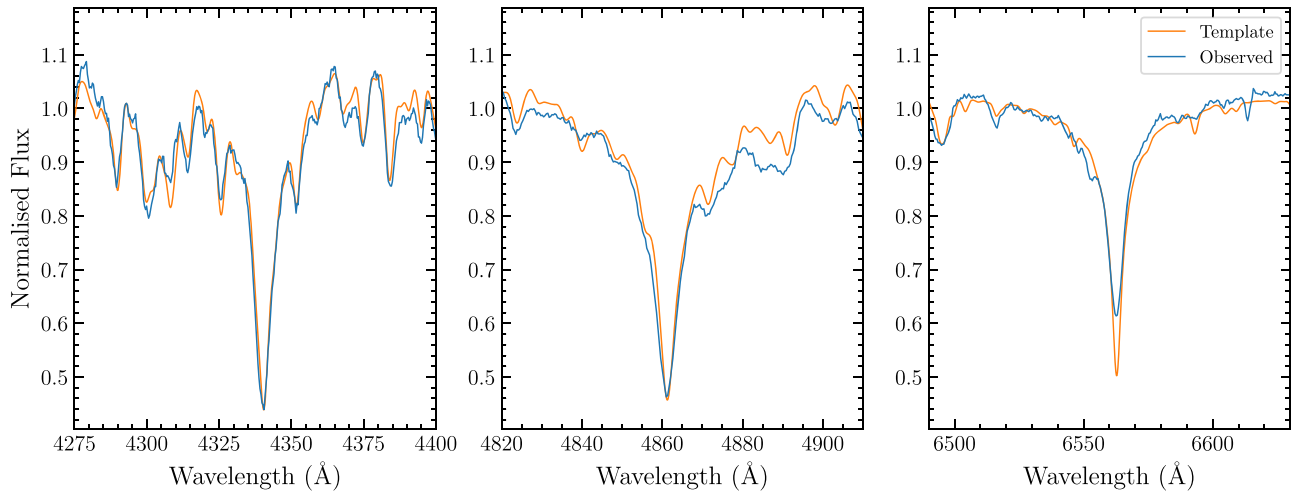
[6] http://pywifes.github.io/pipeline/

Figure 3. Comparison of PHOENIX template ($T_{\rm eff}$ = 6700 K, $\log g$ = 4.0) spectrum with the shifted and averaged spectrum of all observations of Gaia DR3 4042390512917208960. The left, middle, and right panels are cutouts around Hγ, Hβ, and Hα, respectively. Broadly, there is good agreement between the synthetic PHOENIX spectrum and the averaged observed spectrum. Note that the depth of the Hα line is much shallower in the observed spectrum.

averaged background spectrum. To improve signal, for each observation the two exposures were averaged before proceeding to RV estimation, leaving us with 24 RVs spread over 10 months.

RVs were estimated via cross-correlation using the IRAF task FXCOR (Tody 1986, 1993) and a synthetic template spectrum from the PHOENIX library (Husser et al. 2013), which was convolved down to a comparable spectral resolution to the WiFeS data.[7] The library used was the PHOENIX medium-resolution grid with uniform grid spacing of 1 Å. As this spectrum is mainly for determining RVs, and not detailed modeling of the star, we only briefly experimented with metallicity and alpha-element abundances, finding no obvious benefit from the use of nonzero values. The effective temperature ($T_{\rm eff}$) and surface gravity ($\log g$) of Gaia DR3 4042390512917208960 reported in DR3 are 6524^{+31}_{-16} K and $3.804^{+0.002}_{-0.003}$, respectively (Creevey et al. 2023; Fouesneau et al. 2023), corresponding to a spectral type of F4V or F4IV. We matched PHOENIX spectra to the WifeS spectra of the target by eye, finding good agreement between the PHOENIX spectrum with $T_{\rm eff}$ = 6500 K and $\log g$ = 4.0 and the observed spectrum. We found the PHOENIX spectrum with $T_{\rm eff}$ = 6700 K and $\log g$ = 4.0 to be the best match when considering the depths of the absorption lines. The match between the 6700 K template and observation line depth was almost identical for Hβ and Hγ. However, the observed Hα line depth is significantly shallower. Comparisons of the template and observed spectra are shown in Figure 3.

We used the "blue" WiFeS spectra for RV estimation due to the abundance of metal lines. Both Hβ and Hγ were excluded when estimating the RVs to minimize possible contamination arising from emission processes. We used the following regions to estimate RVs with FXCOR: 4200–4300 Å, 4385–4820 Å, and 4900–5400 Å (Figure 4). All velocities were corrected to the solar system barycenter. A systematic uncertainty of 3 km s^{-1} was added to the uncertainty of each estimated RV (Kuruwita et al. 2018). The time of a measured RV was shifted from local observation time to Barycentric Modified Julian Date (BMJD) in the Barycentric Dynamical

Time standard (Eastman et al. 2010). The RV from the SOAR spectrum was estimated in the same way as the WiFeS RVs using the same PHOENIX spectrum and FXCOR. Hα was excluded from the region that was cross-correlated to minimize contamination from emission processes. Furthermore, a correction of 1 km s^{-1} was added based on the telluric oxygen lines in the observation. The estimated RVs for Gaia DR3 4042390512917208960 are presented in Table 1, and the RV from the SOAR spectrum is identified by an asterisk appended to the BMJD. Reported times in Table 1 are the mid-observation time.

3.2. Binary Orbital Parameters

To fit Keplerian orbits to the estimated RVs, we used THE JOKER (Price-Whelan et al. 2017), a custom Monte Carlo sampler designed for this problem. The parameters we consider are the binary orbital period (P), the orbital eccentricity (e), the RV semiamplitude of the luminous star (K), the systemic RV of the binary (γ), a (constant) jitter to account for underestimation of RV errors (s), the argument of periastron (ω), and the orbital phase at the reference time (M_0; by default the reference time used in THE JOKER is the time of the earliest observation). It is important to note that there may be a systematic offset between the WiFeS and SOAR RVs, but with only one SOAR RV we cannot quantify it, and thus we do not attempt to fit for the offset. THE JOKER samples from the prior probability density functions for each parameter we are considering and then performs rejection sampling, producing samples of the posterior for each parameter.

The priors chosen have significant impact on the rejection sampling when the data are sparse or uninformative and should be considered carefully. The observations of Gaia DR3 4042390512917208960 are quite dense and thus the choice of prior is unlikely to significantly affect the results. Nevertheless, we trialed different priors. We used the default prior implemented in the THE JOKER, passing values for the the the standard deviation of the prior on systemic velocity, v_0, and RV semiamplitude, K_0, based on the RVs. We trialed different values to asses the impact of these priors on the final results. We used THE JOKER's default log-normal prior on period, to which we supplied $P_{\min}$ = 0.25 day and $P_{\max}$ = 16384 days as a

---

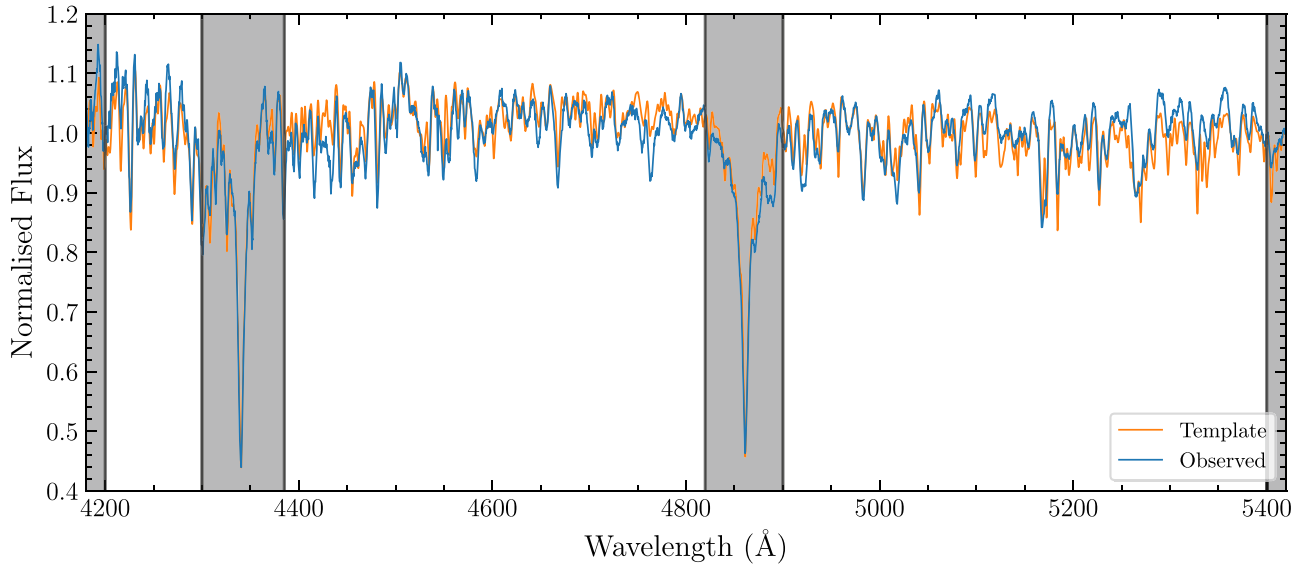[7] http://phoenix.astro.physik.uni-goettingen.de

Figure 4. Comparison of PHOENIX template ($T_{\mathrm{eff}} = 6700$ K, $\log g = 4.0$) spectrum with the shifted and averaged spectrum of all observations of Gaia DR3 4042390512917208960 in the regions used with FXCOR. The shaded regions indicate sections of the spectra that were excluded from the cross-correlation. Note that while we exclude Hγ and Hβ, the region includes prominent lines from many atomic species (e.g., Fe, Ca, Na, and Mg).

Table 1
RVs for Gaia DR3 4042390512917208960 Measured Using Cross-correlation

BMJD	RV (km s^{-1})
59781.6833	19.3 ± 9.0
59810.6610	-41 ± 10
59753.4166	-46.4 ± 9.2
59753.4775	-29.6 ± 7.2
59753.5465	-12.5 ± 6.5
59753.5947	-6.9 ± 6.5
59753.6610	1.2 ± 6.6
59753.6969	6.7 ± 7.1
59781.4678	16.0 ± 7.4
59781.5217	34.6 ± 8.2
59781.5645	29.9 ± 8.2
59781.6163	28.8 ± 8.6
59810.4320	4.0 ± 6.4
59810.4941	-7.3 ± 6.4
59810.5569	-30.0 ± 7.7
59822.4157	-32.8 ± 7.5
59822.4776	-11.9 ± 8.7
59822.5383	-4.3 ± 6.2
59840.4369	-6.0 ± 5.9
59840.4994	-4.6 ± 7.8
59868.4355	34.4 ± 9.6
59882.0102*	-0.2 ± 9.0
60032.7391	-43.4 ± 8.2
60032.7580	-43.7 ± 7.9
60053.7026	32.8 ± 9.5

Note. An asterisk appended to the BMJD indicates the RV was estimated from the SOAR spectrum. The errors in the WiFeS RVs include the 3 km s^{-1} systematic.

Table 2
Orbital Parameters Determined through Modeling the Estimated RVs with a Keplerian Orbit Using the Joker

Parameter	Value
P (day)	$0.89526^{+0.00013}_{-0.00012}$
e	$0.043^{+0.057}_{-0.033}$
K (km s^{-1})	$34.8^{+2.6}_{-2.5}$
γ (km s^{-1})	$-5.3^{+1.7}_{-1.7}$
s (km s^{-1})	$0.0088^{+0.4905}_{-0.0088}$
ω (rad)	$2.6^{+2.0}_{-1.4}$
M_0 (rad)	$-0.7^{+2.0}_{-1.4}$

implemented in PYMC3_EXT. PYMC3_EXT contains PYMC3 (Salvatier et al. 2016) extensions extracted from EXOPLANET (Foreman-Mackey et al. 2021). The priors used here are the same as above, and the results of the rejection sampling are used to initialize the MCMC. Convergence was verified using the Gelman–Rubin diagnostic test (Gelman & Rubin 1992), ensuring the Gelman–Rubin statistic ($\hat{R}$) was close to 1 for all best-fit parameters. We ran 16 chains with 2000 tune iterations and 8000 draws, producing 128,000 final draws.

Changing the standard deviation of the prior on v_0 and K had no impact on inferred values, and neither did the choice of period prior. The periods independently inferred from OGLE photometry and WiFeS RVs are consistent within error, supporting our belief that the spectra are not affected by significant contamination from nearby stars in the Galactic bulge. Therefore, we only present one set of results. The binary orbital parameters inferred from THE JOKER analysis of the RVs are listed in Table 2. While there is some evidence in the posterior for nonzero eccentricity, $e = 0$ cannot be excluded. The 95% upper limit on the eccentricity is 0.18. A comparison between the phase-folded RVs and the best-fitting model, with residuals, is shown in Figure 5.

There is a noticeable scatter in the RVs visible in Figure 5. Additionally, the uncertainty in the RVs determined using FXCOR is larger than we would have expected, based on spectra
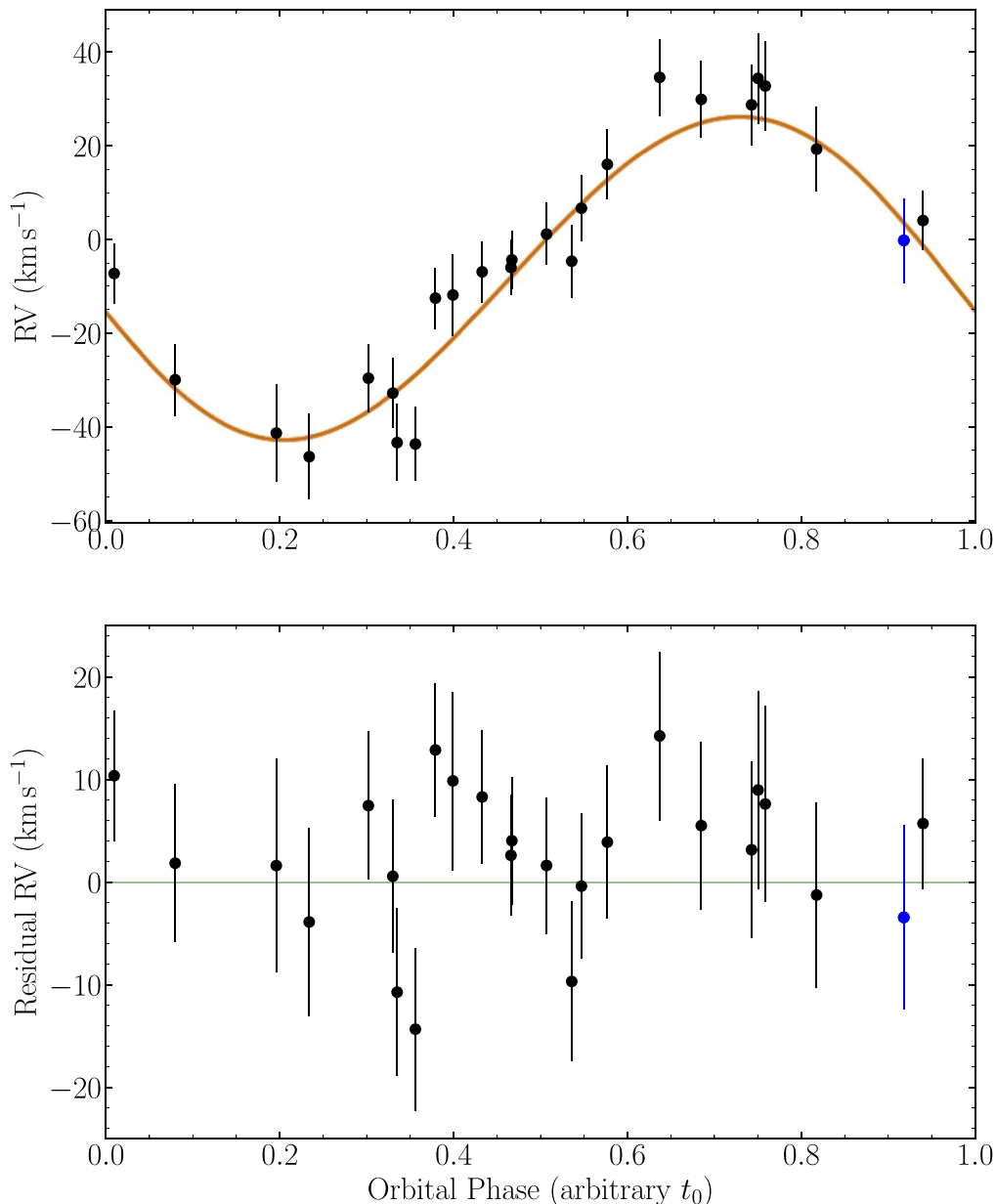
blind search. We also trialed a much narrower prior centered around the orbital period determined from photometry.

When few samples survive and the posterior appears to be unimodal, the posterior samples from the rejection sampling should be used in standard Markov Chain Monte Carlo (MCMC). We used the No-U-Turn Sampling (Hoffman & Gelman 2014) MCMC method to sample the posterior, as

Figure 5. Top: phase-folded RVs overplotted with the best-fit Keplerian model. Bottom: residuals of model minus data as a function of orbital phase. The blue data point is the RV from the SOAR spectrum. The WiFeS RVs are in black.

taken with this instrument of other targets. A plausible explanation for both of these is that the RV from a luminous secondary is causing the scatter. However, excluding spectral disentangling (Section 3.4), we found no evidence for the presence of the secondary in the spectra. It is believed that the WiFeS instrument has a degree of inherent instability (see Kuruwita et al. 2018; the standard deviation of the instability is $\sim 3 \, \mathrm{km \, s^{-1}}$), this could also be contributing to the scatter we see. However, the agreement in orbital period separately determined from photometry and THE JOKER analysis gave us confidence in there being no large systematic issue in the RV modeling.

We then calculated the spectroscopic mass function of the secondary, m_f, using Equation (1):

$$m_f = \frac{M_2^3 \sin^3 i}{(M_1 + M_2)^2} = \frac{P K_1^3}{2\pi G} (1 - e^2)^{3/2}, \qquad (1)$$

where G is the Newtonian constant of gravitation, i is the inclination, M_1 is the mass of the luminous star, M_2 is the mass of the unseen object, and the remaining parameters are as described in Table 2. We used the posteriors from the binary parameter estimation to calculate the mass function of the secondary star $m_f = 3.87^{+0.88}_{-0.77} \times 10^{-3} \, M_\odot$.

3.3. Joint Radial Velocity and Photometry Modeling

Now that we have RVs for Gaia DR3 4042390512917208960, we can model them in conjunction with the excellent OGLE photometry. We started jointly modeling the photometry and RVs using the Eclipsing Light Curve (ELC) code described in Orosz & Hauschildt (2000). Initial results from ELC suggested the binary was composed of two stars, and that both the stars may be filling their Roche lobes, prompting us to switch to PHOEBE (Prša &

Zwitter 2005; Conroy et al. 2020). We trialed different binary configurations using PHOEBE, including detached binaries, semi-detached binaries, binaries on the contact binary boundary (both stars are almost filling their Roche lobe), and contact binaries. We used the period and reference time inferred from the OGLE-IV photometry due to the long time baseline of observations. We calculated the flux from magnitudes using the reference wavelength (λ_{eff}) for the OGLE-IV I-band filter taken from the Spanish Virtual Observatory (Rodrigo et al. 2012; Rodrigo & Solano 2020) assuming OGLE magnitudes are in the AB magnitude system.[8] We selected the logarithmic limb-darkening coefficients of (0.5761, 0.2210) from Claret (2017) using their radial least-squares fit to the log law model for $T_{eff} = 6500$ K and $\log g = 4.0$.

PHOEBE modeling of this system supports the absence of a BH. The large amplitude of the photometric modulation and the low RV semiamplitude of the luminous star are incompatible with the large mass of the unseen object inferred from the photometry using the mMMR. They are also incompatible with a compact object in general. Modeling the system with a NS companion (maintaining orbital and stellar parameters constrained from observations) produces a light curve with a much lower level of photometric modulation, very different light-curve minima, and a much larger RV semiamplitude. These cannot be resolved through inclination effects. A larger amplitude of photometric modulation requires a higher inclination, however decreasing the RV semiamplitude and difference in photometric minima requires a lower inclination. Furthermore, reconciling the observed similarity in photometric minima depths with the high level of photometric modulation is challenging with only a single luminous star due to the physical distortion of the star that is required to recover the large photometric modulation.

When also considering the shape of the light curve, both stars must have a high Roche-lobe filling factor. This places the system on the boundary between a contact binary and a detached binary with high filling factors. We are not able to discern which is the correct interpretation for this system. The similar depth minima in the light curve suggest that each star has a similar temperature. In a contact binary, each star typically has a similar effective temperature and in turn likely has a similar spectrum (e.g., Pribulla et al. 2003; Mitnyan et al. 2020). Assuming a contact binary configuration, we model the system as a contact binary in PHOEBE to constrain system parameters. An inclination and mass ratio of around 60° and 0.2, respectively, seem likely. However, in this configuration, there is an apparent contradiction with previous conclusions: The secondary is contributing a significant amount of flux. This would suggest the observed spectra should be double lined and not single lined as they appear.

3.4. Spectral Disentangling

The joint modeling of the photometry and RVs with PHOEBE led us to infer the spectrum of the unseen companion was hidden in the observed spectrum. To test this, we explored spectral disentangling, using the shift-and-add approach (e.g., González & Levato 2006; Shenar et al. 2020, 2022). When applied to binaries this technique assumes the observed spectra are composites of two individual spectra and exploits that spectral features belonging to each star will move in anti-phase,
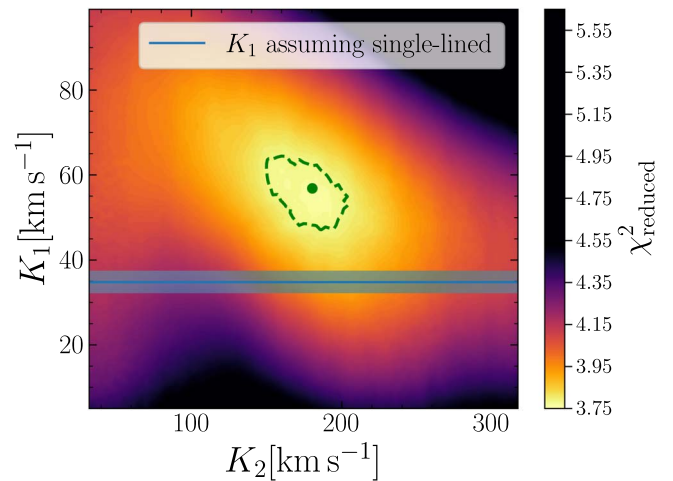
[8] http://svo2.cab.inta-csic.es/svo/theory/fps3/index.php

Figure 6. χ^2 surface explored in the K_1, K_2 grid search, with the green dashed contour indicating 1σ. The semiamplitudes inferred from this exploration were $K_1 = 54.7 \pm 7.2$ km s^{-1} and $K_2 = 177 \pm 21$ km s^{-1}. The K_1 inferred assuming the binary was single lined ($34.8^{+2.6}_{-2.5}$ km s^{-1}) is discrepant with the value inferred using this technique at the 2σ level.

arising from Doppler shifts. If K_1 and/or K_2 are unknown and the other orbital parameters are known, a grid-based exploration can be carried out to infer the K_1, K_2 values that best reproduce the data. This involves evaluating $\chi^2(K_1, K_2)$, the formalism of which is presented in Shenar et al. (2022).

We set the orbital parameters using the period and reference time from OGLE and the systemic velocity from THE JOKER. Eccentricity was set to zero. This choice is motivated by the indications that the system is a contact binary or on the boundary, and that the RVs determined using the method in Section 3.1 are unreliable due to possible smearing (see Section 3.3, and later in this section). We trialed two different explorations of K_1 and K_2. The first was holding K_1 constant as determined with THE JOKER and varying K_2. The second was varying both K_1 and K_2 to investigate the possibility of smearing impacting the RVs inferred using the method described in Section 3.1. The initial guess for this second method was $K_{1,i} = 50$ km s^{-1}, $K_{2,i} = 160$ km s^{-1}, and the grid was split into 100 linearly spaced components between $0.1K_i$ and $2K_i$. We disentangled the regions around Hα, Hβ, Hγ, 4270–4330 Å, and 5150–5200 Å as these are the deepest absorption features in the spectrum. We disentangled these regions independently as well as jointly, and also used the entire spectrum as the disentangling region.

Spectral disentangling reveals this system is likely a double-lined spectroscopic binary (SB2), and not a single-lined spectroscopic binary (SB1) as initially thought. Spectral disentangling while holding K_1 constant suggested the presence of a luminous companion. However, the features in the disentangled spectrum did not correspond to a physically believable stellar spectrum. Therefore, we only present the results of the grid disentangling where both K_1 and K_2 were varied. Disentangling the regions as described above returned consistent values of K_1 and K_2 in all tests, and the resulting disentangled spectrum is consistent with a stellar spectrum. Disentangling all regions excluding Hα (it is not in the "blue" WiFeS spectra) produced $K_1 = 54.7 \pm 7.2$ km s^{-1} and $K_2 = 177 \pm 21$ km s^{-1}. The χ^2 map is shown in Figure 6. The value for K_1 inferred from spectral disentangling is discrepant at the 2σ level with the K_1 inferred assuming the
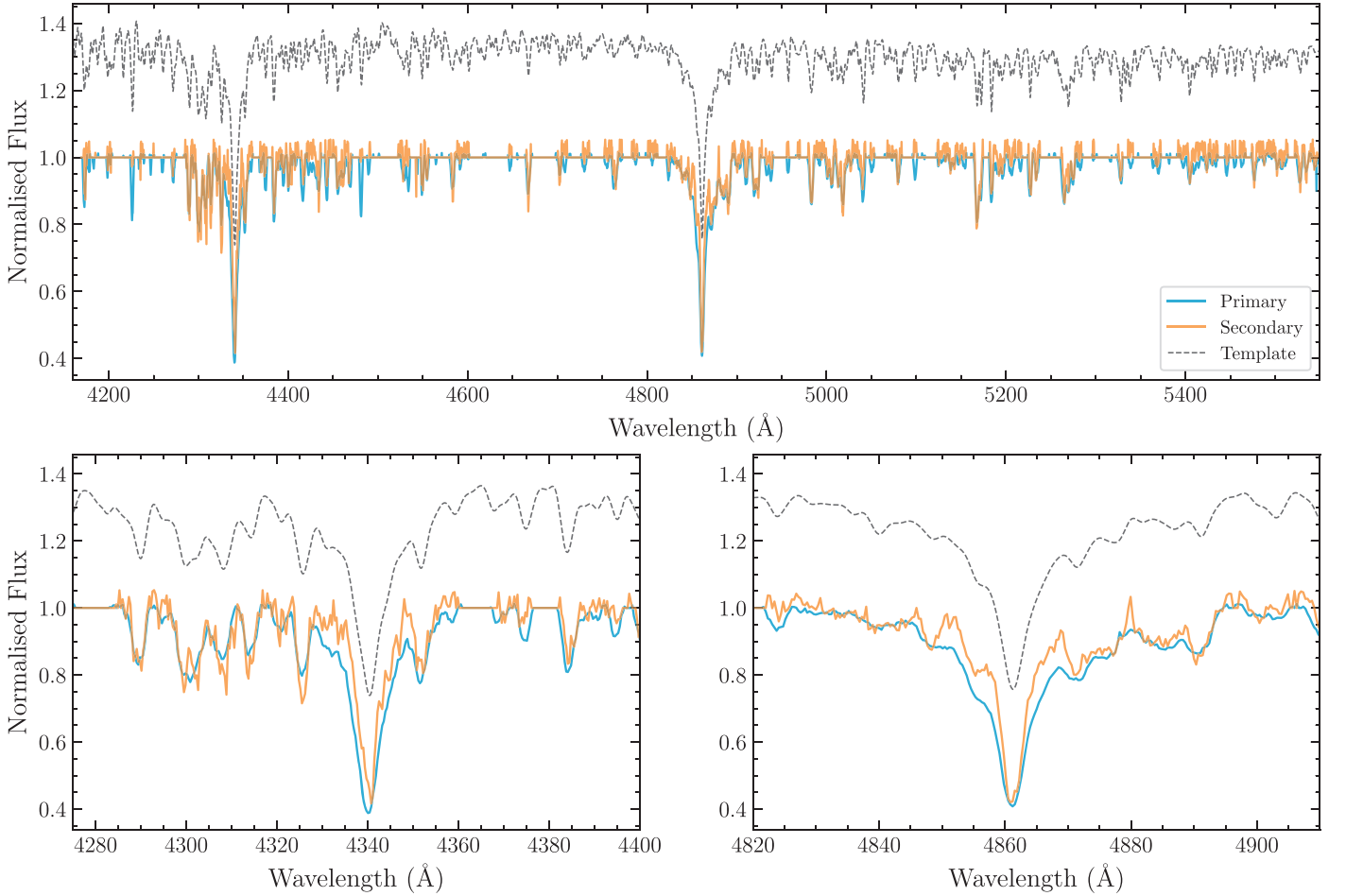
Figure 7. Comparison between the disentangled spectra of the components and the PHOENIX template model identified as the best match to the observed data. The secondary has been scaled for a light ratio such that $l_2/l_{tot} = 0.2$. Noticeably, the disentangled spectra are very similar. The lower-left and right panels are cutouts around Hγ and Hβ, respectively. In all panels the normalized template has been shifted vertically by 0.3 for clarity.

binary is single lined. The disentangled spectrum for each component is presented in Figure 7 along with the PHOENIX template spectrum. They both appear to have a spectral type of either F4V or F4IV, sharing the same prominent lines and species as the spectra discussed in Section 3.1.

4. Discussion

The results inferred from our dedicated spectroscopic campaign and existing photometry imply there is no BH in this system. Considering the RVs in isolation, the system would need to be almost face-on to accommodate a BH. Jointly modeling both RVs and photometry demonstrates that there is no BH in the system, and that the system is more in line with a contact binary or a stellar binary where both stars are almost filling their Roche lobes.

4.1. Radial Velocity Analysis

Based on the spectroscopic mass function alone, the presence of a BH seems unlikely. If we assume the mass of the luminous star in the binary to be $M = 1.7 \pm 0.05\,M_\odot$—the midpoint between the mass estimated by Gaia single-star evolutionary models (Creevey et al. 2023; Fouesneau et al. 2023) and the mass from the PHOENIX template spectrum—the minimum mass of the secondary is $0.25^{+0.02}_{-0.02}\,M_\odot$. This implies that for the secondary to have a mass greater than $3\,M_\odot$

the inclination must be less than $5°$. However, the large photometric variation rules out low inclination angles (Section 3.3). For a conservative lower limit on inclination from the photometry ($i > 50°$), the mass of the primary would have to be greater than $53\,M_\odot$ for the mass of the unseen secondary to be $>3\,M_\odot$. The presence of a BH is therefore ruled out.

However, it is important to consider the results of spectral disentangling discussed in Section 4.2. The RVs inferred as described in Section 3.1 are likely smeared due to the presence of a luminous companion in the spectra. This implies that K and e as inferred through this analysis are likely not reliable. In particular, the eccentricity inferred here should not be used as the basis for an argument against the contact binary scenario. If the eccentricity is truly nonzero, this argues strongly for a detached system with both stars nearly, but not quite, filling their Roche lobes.

4.2. The Single- or Double-lined Nature of the Spectra

Based on the configuration determined using PHOEBE, the secondary is contributing a significant fraction of the light of the system ($>10\%$). However, when visually inspecting the observed spectra we see no evidence for the lines of the secondary. These two conclusions seem mutually exclusive based on the quality of our spectra.

The results of spectral disentangling suggest the system is an SB2 binary, with the spectrum of the secondary buried in the observed spectra. However, the spectra of each component are very similar (Figure 7). Small errors in K_1 can lead to the secondary's disentangled spectrum spuriously mimicking that of the primary (Shenar et al. 2022). However, in our case the K_1 value determined from spectral disentangling is ∼60% larger than the K_1 value determined assuming the spectra are single lined. Furthermore, the disentangled spectrum and the K_1 and K_2 estimates are consistent regardless of the region of the spectra that is used (as stated in Section 3.4). Assuming the secondary contributes 15%–30% of the light (motivated by PHOEBE modeling), we simulated synthetic SB2 spectra with similar resolution, sampling, and signal-to-noise as the observed spectra using the PHOENIX template as the input spectra for both components. Exploring light ratios from 0.0001 to 0.5 supports our results (Appendix). Additionally, the magnitude of K_1 identified from THE JOKER is less than the K_1 identified from spectral disentangling. This is typical behavior when the spectra of both components are blended together (Bodensteiner et al. 2021; Banyard et al. 2022; Shenar et al. 2022). As a result, we are inclined to trust the results of the spectral disentangling analysis. However, we stress that further observations with a higher-resolution spectrograph and more stable instrument are required to confirm the detection of the secondary.

That the disentangled spectra are similar is not surprising if the binary is a contact binary, and in turn provides evidence that the system is a contact binary. While this is a circular argument, it is self-consistent, and in line with all other avenues of investigation for this system. For a detached binary with such a mass ratio it would seem unlikely that both components have such a similar spectrum.

With fitted values for K_1 and K_2 we can determine the mass ratio of the binary. Assuming a circular Keplerian orbit, $q = \frac{K_1}{K_2} = 0.309^{+0.060}_{-0.051}$. Assuming $M_1 = 1.7 \pm 0.05\,M_\odot$ (as discussed in Section 4.1), then $M_2 = 0.525^{+0.103}_{-0.087}\,M_\odot$.

4.3. Discrepant Mass Ratios

The mass ratio determined from spectral disentangling ($0.309^{+0.060}_{-0.051}$) is significantly different than the mMMR of 2.54 determined by assuming the system is an ellipsoidal variable. The mMMR derived by Gomel et al. (2021a) assumes that all the light in the ellipsoidal system is coming from one star, and thus the observed photometric modulation arises due to the distorted star. In the scenario described, and under the assumptions that the star fills its Roche lobe and the binary is observed edge-on, the mMMR is always less than the actual mass ratio. The discrepancy between the mMMR and the mass ratio we determine for Gaia DR3 4042390512917208960 can be explained the same way regardless of whether the system is a contact binary or a binary with both stars being close to filling their Roche lobes. The assumption that all the observed light is coming from a single star breaks down for stellar binaries. In stellar binaries the change in projected surface area as a function of orbital phase is significantly larger than in a star–BH binary due to the presence of two stars. As a result, large modulations can be produced in the light curve purely from the change in projected surface area. As the Gomel et al. (2021a) method assumes the light is coming from one tidally distorted

star, and the mMMR depends primarily on the amplitude of modulation, binaries with two stars will have inflated mMMRs.

Furthermore, this biases samples selected based on high mMMR toward stellar binaries. A random sample of contact binaries will, on average, have higher mMMRs than a random sample of star–BH binaries with the same broad system parameters. If an initial sample of ellipsoidals are contaminated with stellar binaries, then a sample of high-mMMR systems will preferentially include these stellar binaries. The problem is therefore one of classification. While the Gomel et al. (2021a) method appears robust, it is only so if it is applied to true ellipsoidal variables. Reducing the contamination should be the priority of future studies applying the Gomel et al. (2021a) methodology to identify BHs.

4.4. Classification of Gaia DR3 4042390512917208960

The photometry, spectral disentangling, and PHOEBE modeling we have carried out indicate that Gaia DR3 4042390512917208960 is likely a contact binary, or on the boundary with both stars nearly filling their Roche lobes. Classification of the system is not straightforward from photometry alone. It was incorrectly classified as an ellipsoidal variable by Gaia and OGLE, and the initial ASAS-SN variable classification did not have ellipsoidal as a category. However, the system was not identified as an ellipsoidal variable in the later study by Rowan et al. (2021), who used a combined $\chi2$ ratio test followed by visual inspection to analyze ASAS-SN data. Gaia (Eyer et al. 2023) and ASAS-SN (Jayasinghe et al. 2020) used machine-learning classifiers, whereas OGLE (Soszyński et al. 2016) primarily used template fitting. The templates used by the OGLE team were constructed using the OGLE-IV photometry of bright, previously classified ellipsoidal and eclipsing systems in the best-sampled fields. The solution for better discrimination between contact binaries and ellipsoidal variables from photometry alone is also not straightforward. While misclassification is often assumed to be due to sparse data, in the case of Gaia DR3 4042390512917208960, simply having more photometric data is not sufficient to resolve the issue. The OGLE-IV I-band light curve for Gaia DR3 4042390512917208960 has 649 data points spanning a time baseline of more than 2000 days (see Figures 1 and 2), and they also misclassify the system. However, Gaia and OGLE use different methods of classification. Clearly, the classification problem is not limited to one technique, or easily corrected by having more data.

4.5. Contamination of Ellipsoidal Variable Samples

The source studied in this work is either a contact binary or on the boundary with both stars nearly filling their Roche lobes. The 14 systems studied by Nagarajan et al. (2023) are likely contact binaries, and unlikely to host BHs. It seems likely that the contamination of the Gomel et al. (2023) sample with nonellipsoidal systems is very high. As discussed in Section 4.3, when there is contamination, stellar binaries are likely to dominate in samples selected for high mMMR.

Gomel et al. (2023) discussed the difficulty in discriminating between contact binaries and true ellipsoidal systems. They attempted to minimize the contamination by (a) limiting the systems to those with orbital periods >0.25 day, and (b) requiring the light curve to have unequal minima. The periods explored by Nagarajan et al. (2023) extend to 0.75 day, and the

system in this work has a period of 0.8952 day. This suggests that the $P > 0.25$ day restriction is not conservative enough to exclude contact binaries. Furthermore, while unequal minima may help discriminate against other types of variables, it does not exclusively exclude contact binaries and include ellipsoidal variables. Examples of contact binaries with unequal minima include the system studied in this work, systems in Nagarajan et al. (2023) if they are truly contact binaries, and also classical contact binary systems such as 44 Boötis, VW Cephei, and Y Sextantis, which can be seen in Transiting Exoplanet Survey Satellite (Ricker et al. 2015) photometry.

While the mMMR is an excellent technique for identifying candidate compact objects when applied to ellipsoidal variables, the contamination by stellar binaries in the Gomel et al. (2023) sample hampers the viability of using the technique in practice. Further studies should prioritize minimizing contamination by stellar binaries as much as possible before turning to RV studies. Again, we reiterate that removing the contaminating binaries is not a simple problem, as discussed in Section 4.4. Furthermore, while for these studies reliable classification is critical, it is also important that the classification is not computationally expensive. For example, Eyer et al. (2023) analyzed the photometric and spectroscopic time series of 1.8 billion sources from Gaia DR3, identifying 10.5 million sources as variable. In the future, the number of known variables will only grow, and so too will the volume of data available, e.g., from future Gaia data releases, and data from new missions such as the Vera C. Rubin Observatory (Ivezić et al. 2019) and the Nancy Grace Roman Space Telescope (Spergel et al. 2015).

5. Conclusions

We have presented a follow-up investigation of one of the most promising BH candidates from the Gomel et al. (2023) sample of compact object candidates. This sample was identified by leveraging the relationship between optical light-curve modulation amplitude and mass ratio for ellipsoidal variables (Gomel et al. 2021a) and applying it to sources from Gaia DR3. The system we identified as being one of the most interesting candidates from this sample, Gaia DR3 4042390512917208960, had a mMMR of 2.5, implying the unseen secondary was significantly more massive than the luminous star. With detailed multi-epoch spectral observations, we characterized the system, concluding that the binary is unlikely to host a BH. We find the system is most likely a contact binary, with a mass ratio of $0.309^{+0.060}_{-0.051}$, an order of magnitude less than the mMMR. We suggest that this discrepancy arises from the assumption underlying the Gomel et al. (2021a) method that all the light comes from one star and is due to ellipsoidal modulation. In contact binaries there are two stars, which gives rise to a significantly larger change in projected surface area over the binary orbit than for ellipsoidal variables with similar binary system parameters. This causes a larger modulation in the optical light curve and results in an artificially large mMMR. This highlights the main issue with leveraging the Gomel et al. (2021a) technique to find BHs: without better filtering to remove contact binaries (or other stellar binaries), samples selected based on high mMMR are likely to be heavily contaminated. However, while the contact binary interpretation requires a future study to confirm the detection of the secondary's lines, the rationale for the contamination of the Gomel et al. (2021a) sample is still valid

for a detached binary in which both stars are close to filling their Roche lobe. Finally, this work highlights the need for dynamical studies to both confirm new BHs and evaluate exciting new techniques for identifying BH candidates.

Appendix
Spectral Disentangling

Disentangling was performed as described in Section 3.4. The SB2 synthetic data were generated using the PHOENIX template spectrum as the model for each star, reflecting the similarity between the disentangled spectra for Gaia DR3 4042390512917208960. Twenty-four synthetic observations were created to reflect the number of observations of the source, and the model spectra were convolved to a resolution and sampling factor similar to the WiFeS data. The signal-to-noise of the synthetic spectra were set such that the synthetic data were similar to the WiFeS spectra. The same orbital period as Gaia DR3 4042390512917208960 was used, an eccentricity of zero, and $K_1 = 50\,\mathrm{km\,s^{-1}}$ and $K_2 = 160\,\mathrm{km\,s^{-1}}$. The six light contribution fractions (l_2/l_{tot}) examined were 0.5, 0.3, 0.2, 0.1, 0.05, and 0.0001 (reflective of no luminous companion). The K_1, K_2 grid that was explored was quite coarse, split into 15 linearly spaced components between $0.1K_i$ and $2K_i$. For this test, $K_{1,i} = 60\,\mathrm{km\,s^{-1}}$, $K_{2,i} = 192\,\mathrm{km\,s^{-1}}$ to shift the center of the explored grid away from the correct values.

The results presented in Figure 8 suggest we could reliably constrain K_2 and the general shape of the secondary's spectrum when it is contributing $>20\%$ of the total light when both components have the same spectrum. At light contribution fractions of 0.1, 0.05, and 0.0001, the disentangled K_2 is spurious and the disentangled spectrum of the secondary can mimic the primary. The χ^2 surface for light contribution fractions of 0.1, 0.05, and 0.0001 is not smooth and has no clear minima, whereas for light contribution fractions of 0.2, 0.3, and 0.5 the surface is smooth with a clear minimum. The smooth χ^2 map for Gaia DR3 4042390512917208960 (Figure 6) resembles an accurate disentanglement far more than any of the spurious results described in this section. While not conclusive in isolation, we believe it is another piece of supporting evidence that our disentangling results are accurate.
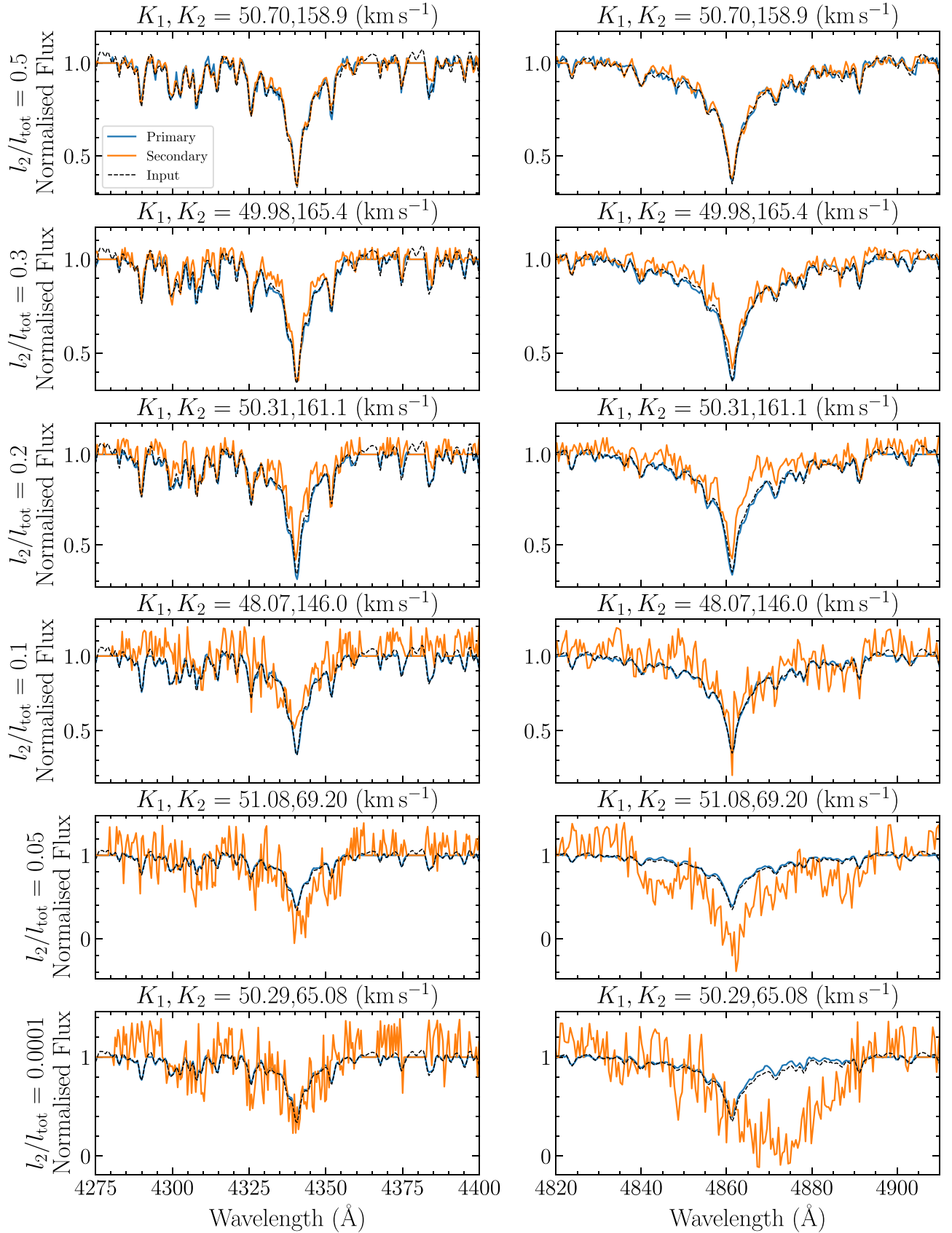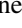
Figure 8. Comparison of disentangled spectra with the input spectrum around Hγ and Hβ for six different light contribution fractions. All secondary spectra are scaled by their light contribution except the bottom row, which is scaled assuming $l_2/l_{tot} = 0.05$. These results suggest that we could reliably detect the presence of a luminous companion if it was contributing at least 20% of the total light of the system.

ORCID iDs

Tyrone N. O'Doherty ⬢ https://orcid.org/0000-0001-9258-1508
Arash Bahramian ⬢ https://orcid.org/0000-0003-2506-6041
Adelle J. Goodwin ⬢ https://orcid.org/0000-0003-3441-8299
James C. A. Miller-Jones ⬢ https://orcid.org/0000-0003-3124-2814
Jerome A. Orosz ⬢ https://orcid.org/0000-0001-9647-2886
Jay Strader ⬢ https://orcid.org/0000-0002-1468-9668

References

Andrew, S., Penoyre, Z., Belokurov, V., Evans, N. W., & Oh, S. 2022, MNRAS, 516, 3661
Astropy Collaboration, Price-Whelan, A. M., Lim, P. L., et al. 2022, ApJ, 935, 167
Banyard, G., Sana, H., Mahy, L., et al. 2022, A&A, 658, A69
Boch, T., & Fernique, P. 2014, in ASP Conf. Ser. 485, Astronomical Data Analysis Software and Systems XXIII, ed. N. Manset & P. Forshay (San Francisco, CA: ASP), 277
Bodensteiner, J., Sana, H., Wang, C., et al. 2021, A&A, 652, A70
Bonnarel, F., Fernique, P., Bienaymé, O., et al. 2000, A&AS, 143, 33
Brown, G. E., & Bethe, H. A. 1994, ApJ, 423, 659
Childress, M. J., Vogt, F. P. A., Nielsen, J., & Sharp, R. G. 2014, Ap&SS, 349, 617
Claret, A. 2017, A&A, 600, A30
Clemens, J. C., Crain, J. A., & Anderson, R. 2004, Proc. SPIE, 5492, 331
Conroy, K. E., Kochoska, A., Hey, D., et al. 2020, ApJS, 250, 34
Corral-Santana, J. M., Casares, J., Muñoz-Darias, T., et al. 2016, A&A, 587, A61
Creevey, O. L., Sordo, R., Pailler, F., et al. 2023, A&A, 674, A26
Dopita, M., Hart, J., McGregor, P., et al. 2007, Ap&SS, 310, 255
Dopita, M., Rhee, J., Farage, C., et al. 2010, Ap&SS, 327, 245
Eastman, J., Siverd, R., & Gaudi, B. S. 2010, PASP, 122, 935
El-Badry, K., & Burdge, K. B. 2022, MNRAS, 511, 24
El-Badry, K., Seeburger, R., Jayasinghe, T., et al. 2022, MNRAS, 512, 5620
El-Badry, K., Rix, H.-W., Cendes, Y., et al. 2023a, MNRAS, 521, 4323
El-Badry, K., Rix, H.-W., Quataert, E., et al. 2023b, MNRAS, 518, 1057
Eyer, L., Audard, M., Holl, B., et al. 2023, A&A, 674, A13
Foreman-Mackey, D., Hogg, D. W., Lang, D., & Goodman, J. 2013, PASP, 125, 306
Foreman-Mackey, D., Luger, R., Agol, E., et al. 2021, exoplanet: Gradient-based Probabilistic Inference for Exoplanet Data & Other Astronomical Time Series, v0.5.1, Zenodo, doi:10.5281/zenodo.1998447
Fouesneau, M., Frémat, Y., Andrae, R., et al. 2023, A&A, 674, A28
Gaia Collaboration, Prusti, T., de Bruijne, J. H. J., et al. 2016, A&A, 595, A1
Gaia Collaboration, Vallenari, A., Brown, A. G. A., et al. 2023, A&A, 674, A1
Gavras, P., Rimoldini, L., Nienartowicz, K., et al. 2023, A&A, 674, A22
Gelman, A., & Rubin, D. B. 1992, StaSc, 7, 457
Giesers, B., Dreizler, S., Husser, T.-O., et al. 2018, MNRAS, 475, L15
Giesers, B., Kamann, S., Dreizler, S., et al. 2019, A&A, 632, A3
Gomel, R., Faigler, S., & Mazeh, T. 2021a, MNRAS, 504, 2115
Gomel, R., Faigler, S., Mazeh, T., & Pawlak, M. 2021b, MNRAS, 504, 5907
Gomel, R., Mazeh, T., Faigler, S., et al. 2023, A&A, 674, A19
González, J. F., & Levato, H. 2006, A&A, 448, 283
Harris, C. R., Millman, K. J., van der Walt, S. J., et al. 2020, Natur, 585, 357
Hoffman, M. D., & Gelman, A. 2014, JMLR, 15, 1593
Hunter, J. D. 2007, CSE, 9, 90
Husser, T. O., Wende-von Berg, S., Dreizler, S., et al. 2013, A&A, 553, A6
Ivezić, Ž., Kahn, S. M., Tyson, J. A., et al. 2019, ApJ, 873, 111
Jayasinghe, T., Stanek, K. Z., Kochanek, C. S., et al. 2020, MNRAS, 491, 13

Joye, W. A., & Mandel, E. 2003, in ASP Conf. Ser. 295, Astronomical Data Analysis Software and Systems XII, ed. H. E. Payne, R. I. Jedrzejewski, & R. N. Hook (San Francisco, CA: ASP), 489
Kochanek, C. S., Shappee, B. J., Stanek, K. Z., et al. 2017, PASP, 129, 104502
Kuruwita, R. L., Ireland, M., Rizzuto, A., Bento, J., & Federrath, C. 2018, MNRAS, 480, 5099
Lam, C. Y., Lu, J. R., Udalski, A., et al. 2022a, ApJS, 260, 55
Lam, C. Y., Lu, J. R., Udalski, A., et al. 2022b, ApJL, 933, L23
Lindegren, L., Klioner, S. A., Hernández, J., et al. 2021, A&A, 649, A2
Mahy, L., Sana, H., Shenar, T., et al. 2022, A&A, 664, A159
McKinney, W. 2010, in Proc. Python in Science Conf., ed. S. van der Walt & J. Millman (Austin, TX: SciPy), 56
Mitnyan, T., Szalai, T., Bódi, A., et al. 2020, A&A, 635, A89
Nagarajan, P., El-Badry, K., Rodriguez, A. C., van Roestel, J., & Roulston, B. 2023, MNRAS, 524, 4367
Olejak, A., Belczynski, K., Bulik, T., & Sobolewska, M. 2020, A&A, 638, A94
Orosz, J. A., & Hauschildt, P. H. 2000, A&A, 364, 265
Perez, F., & Granger, B. E. 2007, CSE, 9, 21
Pribulla, T., Kreiner, J. M., & Tremko, J. 2003, CoSka, 33, 38
Price-Whelan, A. M., Hogg, D. W., Foreman-Mackey, D., & Rix, H.-W. 2017, ApJ, 837, 20
Prša, A., & Zwitter, T. 2005, ApJ, 628, 426
Ricker, G. R., Winn, J. N., Vanderspek, R., et al. 2015, JATIS, 1, 014003
Riello, M., De Angeli, F., Evans, D. W., et al. 2021, A&A, 649, A3
Rimoldini, L., Holl, B., Gavras, P., et al. 2023, A&A, 674, A14
Rodrigo, C., & Solano, E. 2020, XIV.0 Scientific Meeting (Virtual) of the Spanish Astronomical Society (Madrid: La Sociedad Española de Astronomía), 182, https://www.sea-astronomia.es/reunion-cientifica-2020
Rodrigo, C., Solano, E., & Bayo, A. 2012, SVO Filter Profile Service, v1.0, IVOA, doi:10.5479/ADS/bib/2012ivoa.rept.1015R
Rowan, D. M., Stanek, K. Z., Jayasinghe, T., et al. 2021, MNRAS, 507, 104
Sahu, K. C., Anderson, J., Casertano, S., et al. 2022, ApJ, 933, 83
Salvatier, J., Wieckiâ, T. V., & Fonnesbeck, C., 2016 PyMC3: Python Probabilistic Programming Framework, Astrophysics Source Code Library, ascl:1610.016
Samland, M. 1998, ApJ, 496, 155
Saracino, S., Kamann, S., Guarcello, M. G., et al. 2022, MNRAS, 511, 2914
Saracino, S., Shenar, T., Kamann, S., et al. 2023, MNRAS, 521, 3162
Shahaf, S., Bashi, D., Mazeh, T., et al. 2023, MNRAS, 518, 2991
Shappee, B. J., Prieto, J. L., Grupe, D., et al. 2014, ApJ, 788, 48
Shenar, T., Bodensteiner, J., Abdul-Masih, M., et al. 2020, A&A, 639, L6
Shenar, T., Sana, H., Mahy, L., et al. 2022, A&A, 665, A148
Soszyński, I., Pawlak, M., Pietrukowicz, P., et al. 2016, AcA, 66, 405
Spergel, D., Gehrels, N., Baltay, C., et al. 2015, arXiv:1503.03757
Stevance, H. F., Parsons, S. G., & Eldridge, J. J. 2022, MNRAS, 511, L77
Tanikawa, A., Hattori, K., Kawanaka, N., et al. 2023, ApJ, 946, 79
Tetarenko, B. E., Sivakoff, G. R., Heinke, C. O., & Gladstone, J. C. 2016, ApJS, 222, 15
Thompson, T. A., Kochanek, C. S., Stanek, K. Z., et al. 2019, Sci, 366, 637
Thompson, T. A., Kochanek, C. S., Stanek, K. Z., et al. 2020, Sci, 368, eaba4356
Timmes, F. X., Woosley, S. E., & Weaver, T. A. 1996, ApJ, 457, 834
Tody, D. 1986, Proc. SPIE, 627, 733
Tody, D. 1993, in ASP Conf. Ser. 52, Astronomical Data Analysis Software and Systems, ed. R. J. Hanisch, R. J. V. Brissenden, & J. Barnes (San Francisco, CA: ASP), 173
Udalski, A., Szymański, M. K., & Szymański, G. 2015, AcA, 65, 1
van den Heuvel, E. P. J. 1992, Environment Observation and Climate Modelling Through International Space Projects SEE N93-23878 08-88, ESA
Virtanen, P., Gommers, R., Oliphant, T. E., et al. 2020, NatMe, 17, 261
Wenger, M., Ochsenbein, F., Egret, D., et al. 2000, A&AS, 143, 9
Wiktorowicz, G., Wyrzykowski, Ł., Chruslinska, M., et al. 2019, ApJ, 885, 1